Featured in Physics

Closed-Loop Control of Active Nematic Flows

Katsu Nishiyama,[*] John Berezney,[*] Michael M. Norton,[*] Akshit Aggarwal, Saptorshi Ghosh, Zahra Zarei, Michael F. Hagan, and Seth Fraden[†]

The Martin Fisher School of Physics, Brandeis University, Waltham, Massachusetts 02454, USA

Zvonimir Dogic

Department of Physics, University of California, Santa Barbara, California 93106, USA, and Interdisciplinary Program in Quantitative Biosciences, University of California, Santa Barbara, California 93106, USA

(Received 13 March 2025; accepted 9 October 2025; published 19 December 2025)

Stabilizing and shaping autonomous flows of active fluids is a fundamental challenge and a prerequisite for applications. We embed a light-responsive microtubule-based nematic in a proportional-integral control loop that adjusts the applied light intensity in response to real-time measurements of the spatially averaged flow speed. The self-regulating hardware-software-wetware system maintains a target flow speed against external or internal perturbations, including protein aging and aggregation, sample-to-sample variability, and temperature variation. Varying the controller's gains reveals antagonistic roles between feedback and intrinsic processes, leading to nontrivial dynamics observed in fluctuation spectra. In particular, oscillations emerge from the interplay between the controller, motor binding kinetics, and active hydrodynamic relaxation. Accounting for the underlying binding timescale, our coarse-grained model and nematohydrodynamics simulations corroborate these observations. This work provides insight into the coupled dynamics of controlled active matter, laying the foundation for spatiotemporal patterning of active stress to generate and stabilize new dynamical configurations.

DOI: 10.1103/4hrx-6rdq

Subject Areas: Fluid Dynamics, Materials Science, Soft Matter

I. INTRODUCTION

Living systems exhibit complex dynamical behaviors that are robust against external and internal perturbations. This resilience emerges from endogenous feedback mechanisms that continuously reinforce functional attractor states, managing essential physiological processes such as cell division, motility, and morphogenesis [1–5]. These exquisite yet robust dynamical behaviors inspired efforts to create analogous synthetic materials. A promising route involves reconstituting nonequilibrium systems from purified cytoskeletal components. The resulting materials exhibit diverse dynamics ranging from aster formation, bulk contractions, flocking transitions, active nematic liquid crystals, active foams, and spontaneously flowing active fluids [6–15]. However, while bottom-up designs replicate certain features of living matter, they lack engineered control mechanisms for autonomous stability or dynamical state transitions [16]. Moreover, achieving a target behavior is challenging because such far-from-equilibrium materials tend to be unstable, exhibiting chaotic dynamics and spontaneous switching among multiple coherent states [17–19]. Incorporating control into active matter holds the potential not only to stabilize the system against perturbations, but also to direct its dynamical evolution, thereby opening new frontiers in materials science and synthetic biology [20].

New dynamics of active matter can emerge in confined geometries [21–33], patterning viscosity or anisotropy of the underlying layer [34,35], variation of spatial adenosine triphosphate (ATP) concentration or protein inhibitor [36–38], and applied external flows [39]. However, these methods generate dynamics that is largely predetermined and cannot be easily altered during the experiment. Photoactivable motor proteins enable spatiotemporal control of active matter, opening the possibility of programmable behaviors that were previously inaccessible [40–46]. Such goals require theoretical prescription for control inputs that will steer the system toward the desired target. At the level of hydrodynamics, optimal control and

[*]These authors contributed equally to this work.

[†]Contact author: fraden@brandeis.edu

physics-informed methods that reduce the dimensionality of the control space have demonstrated potential [47–52]. At the discrete level, optimal control yields inputs that guide individual particle trajectories and ensembles [53–55]. Machine learning-based reinforcement learning and physics-informed neural networks provide alternative methods for generating control policies that do not rely on preexisting theoretical models [56–59]. However, even the most carefully designed strategies suffer from model mismatch, unknown parameters, and degradation of the biomolecular constituents over time, hindering practical implementations.

A time-tested approach to address these limitations is to continuously remeasure and recalculate control inputs [60]. Thus, feedback is an indispensable feature, but one that has heretofore been unaddressed in the context of active continua despite the successful implementation of model-informed feedforward control [44,45]. Motivated by these considerations we implement proportional-integral (PI) feedback to stabilize active nematics flows against external temperature perturbations and internal protein-induced degradation and drift. The feedback scheme enables rapid switching between different target dynamics and controls the magnitude of the intrinsic fluctuations of active nematics. Theory and numerics provide a quantitative foundation for controlling the dynamics of active liquid crystals. The power spectra of activity-driven hydrodynamic fluctuations reveals a complex interplay between the system's intrinsic timescales and controller gains. Notably, this coupling leads to reentrant transitions between underdamped and overdamped dynamics. Our work underscores the importance of coupling theory and experiment to develop adaptive, nonequilibrium materials with tailored functionalities. Beyond active fluids, the developed methods could be applied to other photoresponsive systems, including active colloids [61,62], bacteria [63–65], and microswimmers [66–68].

II. RESULTS

A. Microtubule-based active nematics

We study two-dimensional active nematics assembled from microtubules driven by clusters of light-activated kinesin molecular motors [40,42,43,69]. The high microtubule density promotes local nematic alignment, while the extensile stresses generated by molecular motors amplify the local bend deformations [9,70], creating motile topological defects and large-scale chaotic material flows [71,72]. While these nonequilibrium materials reach quasi-steady-state behavior within minutes of activation, they often exhibit long-term drifts from degradation or proteins and/or fluctuations in environmental conditions. Light-activated nematics have poor reproducibility. Their speed is sensitive to temperature variations [Fig. 1(b)] [36], as well as high sample-to-sample variations, as well as the variation in speed of a single sample over time as the material ages [Figs. 2(d)–2(f)]. In contrast, living matter

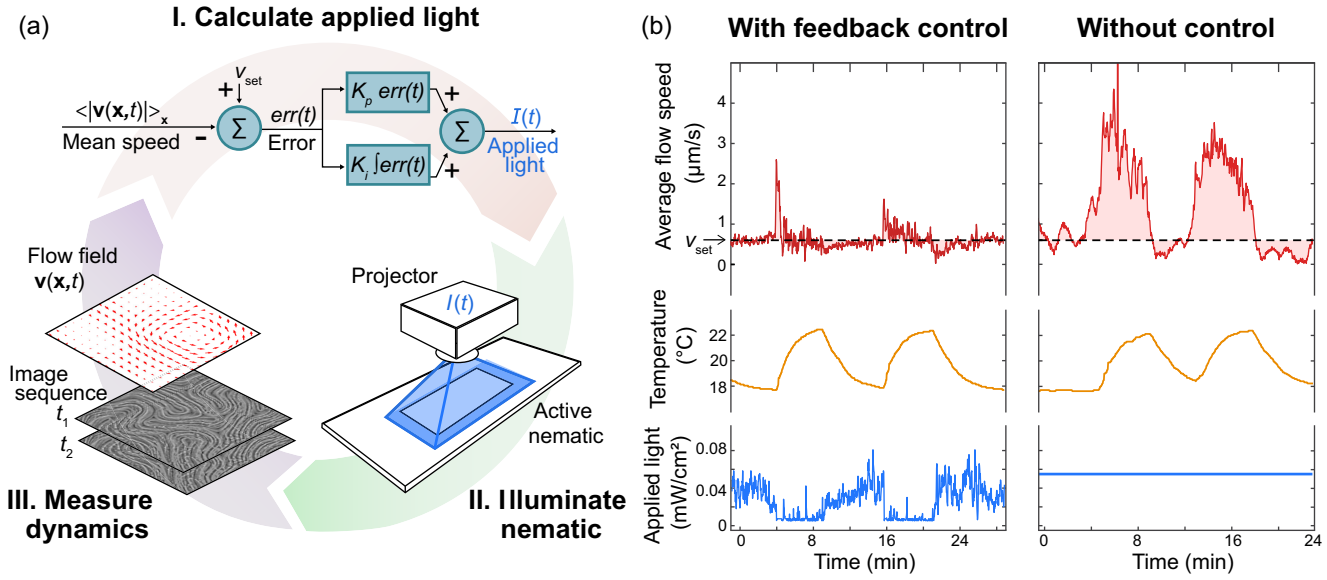

FIG. 1. Feedback control regulates active nematic flows. (a) Integration of hardware, wetware, and software into a control system. (a)(I) A PI control algorithm adjusts the applied light to regulate the mean speed. (a)(II) A spatially uniform light field with time-varying intensity is projected onto the sample, where light-sensitive kinesin motors drive the active nematics flows. (a)(III) The system state is measured by fluorescence video microscopy. Optical flow generates a vector flow field [73], which is reduced to the mean speed. (b) Variation of the nematic speed relative to its set point, with and without feedback control, during two cycles of time-varying temperature. The applied light automatically decreases as temperature increases and vice versa to minimize the error. The average magnitude of deviation from the set point under control is 4.3 times less than without control. Control parameters: $K_p^* = 7.1$ and $K_i^* = 0.071\,\mathrm{s}^{-1}$.

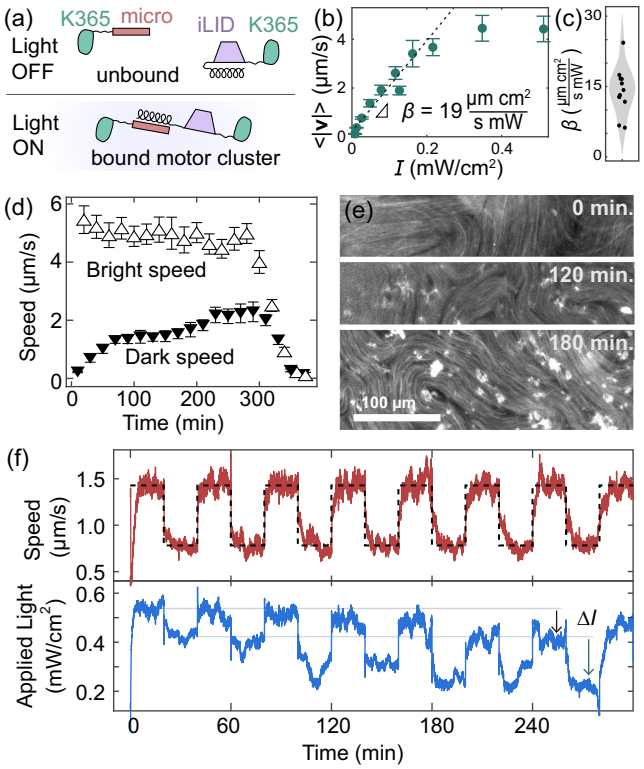

FIG. 2. PI control adapts to the aging of an active nematic and rapidly switches between set points. (a) The application of light reduces the dissociation constant of the light-responsive kinesin fusion proteins, K365-iLID and K365-micro, promoting the formation of heterodimeric motor clusters. (b) Incorporation of motor proteins in a 2D nematic generates light-dependent flows whose speed increases linearly between 0 and 0.15 mW cm^{-2}. (c) Experimental scatter between sample preparations leads to differences in β with an average of 14.0 μm s^{-1} cm^2 mW^{-1} and standard deviation of 4.6 μm s^{-1} cm^2 mW^{-1}. (d) The dynamic range of the flow decreases over time due to both a reduction in maximum speed and an increase in minimum speed. (e) Significant aggregation occurs over time, evidenced by the accumulation of large irregular clusters of tubulin. Similar aggregation is seen in the motor clusters (Fig. S1 in SM [74]). (f) The control system successfully maintains a set mean speed, and rapidly acquires a new mean speed upon changing the set point. The PI control algorithm adjusts the applied light to compensate for changes in the light response of the system over time (SM Movie 1 [74]). Data represented in (b), (d), and (f) are derived from different experiments and therefore exhibit quantitative differences in measurements.

maintains self-regulating homeostasis, which stabilizes target dynamics despite perturbations. We use feedback to control the speed of active nematics.

B. Demonstration of control

We developed a hybrid hardware-software system that integrates real-time imaging and analysis with optical stimulation [Fig. 1(a)]. Our platform features a light source that projects spatially and temporally varying light patterns onto the light-responsive active nematic. The system continuously acquires high-resolution images of the active nematic, which are processed in real time to extract the two-dimensional flow field, orientation field, and positions of topological defects. All components, including microscopy, device control, image processing, and feedback algorithms, are controlled by custom PYTHON scripts, providing a flexible framework that accommodates a wide range of tasks.

We use proportional-integral feedback to stabilize the spatially averaged flow speed $v = \langle|\mathbf{v}(\mathbf{x},t)|\rangle_{\mathbf{x}}$ at a target magnitude v_{set} [Fig. 1(a)]. The light projector applies a uniform light field across the entire active nematic sample, producing spatially uniform motor cluster binding. Machine learning-based optical flow measures the flow field from two sequential images captured one second apart [73]. Similar performance can likely be achieved using conventional particle image velocimetry algorithms. Subsequently, the feedback cycle is completed by calculating the spatially averaged flow speed of the nematic and feeding this value back into the control algorithm to adjust the projected light intensity.

As a demonstration of our system, we show its ability to maintain a target speed under large applied thermal perturbations [Fig. 1(b)]. Kinesin-motor stepping and, consequently, active nematic flow speeds, are sensitive to temperature variations [36]. In the absence of control, thermal cycling induces large and persistent deviations in speed [Fig. 1(b)]. When under control, the speed trajectory remains close to the set speed, exhibiting little deviation, despite the applied heat perturbations. The time trajectory of the applied light highlights the controller's ability to dynamically adjust the applied light to compensate for system changes.

C. PI control and light response calibration

We accomplish our control objectives by implementing a minimal, model-free proportional-integral control law,

$$I = K_{\text{p}}(v_{\text{set}} - v) + K_{\text{i}}\int_0^t (v_{\text{set}} - v)dt', \qquad (1)$$

where I is the applied light intensity determined by the sum of two contributions: one proportional to the instantaneous error, $\text{err}(t) = v_{\text{set}} - v$, and the other proportional to the integrated time history of the error. K_{p} and K_{i} control "gains" that dictate the magnitude of the contributions of the two terms. The PI control allows for the light intensity to be negative. However, as this is experimentally unfeasible, the light intensity is set to its minimum value, ensuring uninterrupted regulation of the nematic speed.

The response of the system to applied light arises from the reversible light-dependent binding of kinesin-motor proteins [K365-micro and K365-iLID; Fig. S1 in Supplemental Material (SM)] into heterodimeric motor

clusters [Fig. 2(a)] [74]. In the absence of light, unbound kinesin monomers walk freely on microtubules but do not create large-scale material reconfiguration. Light induces formation of motor clusters, which in turn drive relative sliding between adjacent microtubules, generating large-scale nematic flows. Thus, light serves as a "clutch," engaging and disengaging the transmission of nanoscale motion to macroscopic material flows.

The speed of the photoresponsive active nematic increases linearly with light at low intensities [Fig. 2(b), $\beta = 18.7 \mu m s^{-1} cm^2 mW^{-1}$]. Within this regime (0–0.15 $mWcm^{-2}$), the steady-state speed follows $v_{ss} \sim \beta I_{ss}$. At higher intensities, the speed saturates. The biomolecular constituents are susceptible to degradation, aggregation, and sample-to-sample variability. Consequently, β varies between samples by 40%, posing challenges for open-loop control design [Fig. 2(c)]. Furthermore, within a single sample, the light response degrades over time as motors and microtubules aggregate [Figs. 2(d) and 2(e) herein and Fig. S1 in SM [74]]. These observations highlight the limitations of an open-loop approach, as the lack of a fixed relationship between light intensity and speed prevents reproducible dynamics.

The feedback control reliably switched between different steady-state dynamics. We set a target speed that followed a square wave trajectory [Fig. 2(f) (black)]. Unlike open-loop control, which failed to correct for degradation and drift, the PI controller continuously adjusted the applied light intensity to compensate for long-term drift in the response [Fig. 2(f) (blue)]. As a result, the measured speed followed the prescribed trajectory, while also responding dynamically to the intrinsic hydrodynamic fluctuations of the nematic [Fig. 2(f) (red)].

D. Tuning control parameters

Complex dynamics emerges from the interactions between a controller and a system's intrinsic behaviors. For example, PI controllers can induce oscillatory behavior in otherwise overdamped systems [60]. Thus, while PI controllers are ubiquitous, due to being model-free, effective, and simple to implement, they are successful only when properly tuned. Controlling active systems introduces further nuances due to their intrinsic fluctuations. Next, we study controlled active nematics by systematically varying K_i and K_p.

We compare our results to two theoretical models. The first is an empirically motivated linear model governed by two intrinsic timescales: the coarse-grained mean speed's relaxation τ_v and the motor binding dynamics τ_m [Eqs. (B1) and (B2) in Appendix B]. The model predicts the steady-state speed [v_{ss}^*, Eq. (B4)] and the spectral characteristics of its fluctuations [Eq. (B5)]. These steady-state expressions include the susceptibility of the nematic speed to applied light, or β, which is experimentally measured [Fig. 2(b)]. Knowing β and the control gains allows us to compare

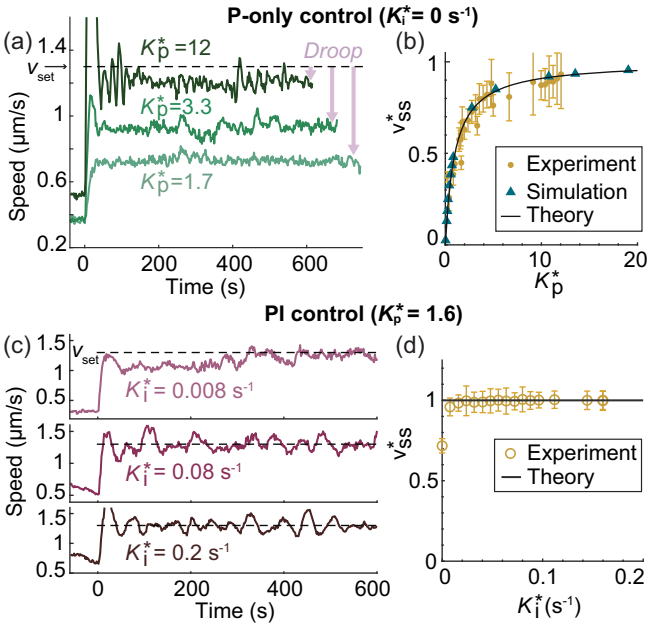

FIG. 3. Varying the PI control parameters (SM Movies 2 and 3 [74]). (a) Response of system with varied K_p^*, $K_i^* = 0$ and with a set speed of 1.3 $\mu m\, s^{-1}$, where $K_{p,i}^* = \beta K_{p,i}$ and β is the proportionality such that $v_{ss} \sim \beta I$; see Fig. 2(a). (b) Steady-state speed v_{ss}^* approaches the set point at large proportional gain with agreement between experiment, simulation, and theoretical predictions, Eq. (B4). (c) Response of system at set speed of 1.3 $\mu m\, s^{-1}$ with varied integral gain terms. (d) Steady-state droop disappears when the integral term is used.

results between theory and experiment as a function of rescaled gains $K_{p,i}^* = \beta K_{p,i}$ (Appendix B). Second, we also compare results to numerical simulations of the full nematohydrodynamic equations subject to the same control law Eq. (1) and motor dynamics Eq. (B2). Here, too, a measurement of β *in silico* enables comparison.

We first consider proportional-only control by systematically varying K_p^* while setting $K_i^* = 0$. In proportional control, the output light intensity varies linearly with the instantaneous deviation of the measured speed from the set point. This control law generates steady-state error, known as droop, where the measured speed is systematically lower than the target speed by a constant value. We found that experimentally measured droop increases with decreasing K_p^* [Fig. 3(a)]. Droop is a generic feature of proportional-only control. Thus, it provided a robust benchmark for comparing experiments to the analytical model and simulation. With increasing gain, the dimensionless steady-state speed v_{ss}^* [Eq. (B4), Appendix B] asymptotically and monotonically approaches the set speed. Without fitting parameters, this is in excellent agreement with results from experiment and simulation [Fig. 3(b)].

Proportional-only feedback requires large gains to approach target set points, which often induce large overshoots [$K_p^* = 12$ curve in Fig. 3(a)]. Introducing the

integral control term regulates the dynamics, that attains the exact target speed by accumulating the error over time and adjusting the control to bring the offset to zero. Any amount of K_i drives the system to the set point, but faster equilibration required larger K_i [Figs. 3(c) and 3(d)]. Notably, while introducing K_i removes droop, high values of K_i generate oscillations [Fig. 3(c)]. This behavior can be evaluated throughout parameter space. A phase diagram describing both the timescale of approach to the set point and the frequency of oscillation demonstrates an optimal combination of K_p and K_i that rapidly approaches the set point (Fig. S5) [74]. Thus, carefully tuned gain parameters are critical for optimal dynamics.

E. Spectral response of system to PI control

We showed that PI control regulates the spatially averaged flow speed of an active nematic. However, there are significant temporal fluctuations that strongly depend on the control parameters. To illustrate, we perform experiments in which the controller switches between on and off states (Fig. 4). When engaged, the controller actively manages the applied light in response to measured dynamics; when disengaged, a constant light intensity is applied, determined by the average of the previous closed-loop window. The resulting speed trajectory and histogram shows that the amplitude and timescale of the set point deviations are strongly impacted by the feedback loop [Figs. 4(a) and 4(b)].

To understand these fluctuations, we compute their power spectral density, PSD(v). In the absence of control, the PSD(v) exhibits white noise fluctuations at low frequencies, transitioning to a power law above a corner frequency [dashed black line in Fig. 5(a)]. This establishes a baseline against which we compare the effects of applied control. Our model produces the same Lorentzian-like response, where the corner frequency f_v is inversely related to v's relaxation time such that $f_v = (2\pi\tau_v)^{-1}$ [Eqs. (B1) and (B2)]. Interestingly, these dynamics do not exhibit a

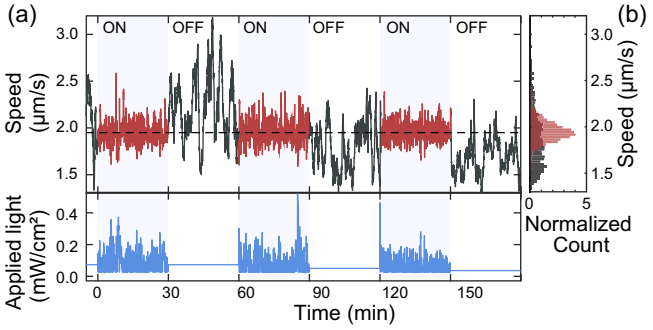

FIG. 4. Control affects fluctuations of active nematics. (a) Intermittent PI control shows the impact of the controller on the amplitude and timescale of fluctuations (SM Movie 4 [74]). (b) Histogram of fluctuations of mean speed with PI control (red) and without (black).

signature of the internal timescale associated with kinesin-motor cluster formation (τ_m). However, this timescale emerges when the controller is engaged and its action couples with the system's response.

The addition of control decreases the fluctuations from the set point, leading to a decrease in the amplitude of the PSD(v) compared to uncontrolled samples. However, the suppression of fluctuations is not uniform across the spectra. We explored the frequency response for proportional-only [Figs. 5(a) and 5(b)] and proportional-integral [Figs. 5(d) and 5(e)] control for a range of K_p values. For example, increasing K_p strongly attenuates the low-frequency fluctuations [Figs. 5(a) and 5(d)], which is corroborated by theory [Figs. 5(b) and 5(e)].

The heterogeneous action of the controller across timescales becomes particularly evident at large gains, where it gives rise to peaks at selected frequencies, indicative of oscillatory dynamics. Experimentally, the PSD(v) displays peaks near $f \sim (1 \times 10^{-2}$ Hz$)$ for sufficiently large K_p values [Figs. 5(a), 5(b), 5(d), and 5(e)]. The emergence of these peaks corresponds to a transition from overdamped to underdamped behavior, which is also captured in the autocorrelation function (Fig. S2 [74]). The linear ordinary differential equation model clarifies that these coherent fluctuations result from the interaction between the controller and the intrinsic motor response timescale of the active nematic [Eqs. (B1) and (B2)]. Notably, in the analytical model the motor dynamics time lag is essential for creating oscillations under proportional-only control. By contrast, oscillations do not emerge if control acts directly on the velocity field. In this case the dynamics Eq. (B1) reduces to $\dot{v} = -v/\tau_v + \gamma K_p(v_{set} - v)$ and the single eigenvalue is real. Oscillations distinguish PI control of active nematics from simpler overdamped systems, highlighting the importance of incorporating motor dynamics into predictive models.

Both experiment and theory identify distinct regions of parameter space ($\{K_p^*, K_i^*\}$) corresponding to overdamped and underdamped responses [Fig. 5(c)]. The boundary between these is theoretically predicted by examining the eigenvalues λ of the combined PI-nematic system [Eq. (B6)]. The wedge-shaped region's interior corresponds to overdamped behavior [Im$(\lambda) = 0$] whereas the exterior region supports oscillations [Im$(\lambda) > 0$]. Experimental observations of overdamped and underdamped responses are consistent with this behavior. Integral control can turn overdamped systems into harmonic oscillators. However, we observe oscillations for large K_p, highlighting the importance of motor dynamics, as oscillations are possible only if intrinsic dynamics are second order or higher. This facet of the system-controller dynamics gives rise to the reentrant phase diagram [Figs. 5(c) and 5(f)].

We attribute the measurement scatter to sample variation and aging, which affects the positions of points in the plot. Notably, oscillations dominate much of the parameter space suggesting that only a narrow range of parameters may be

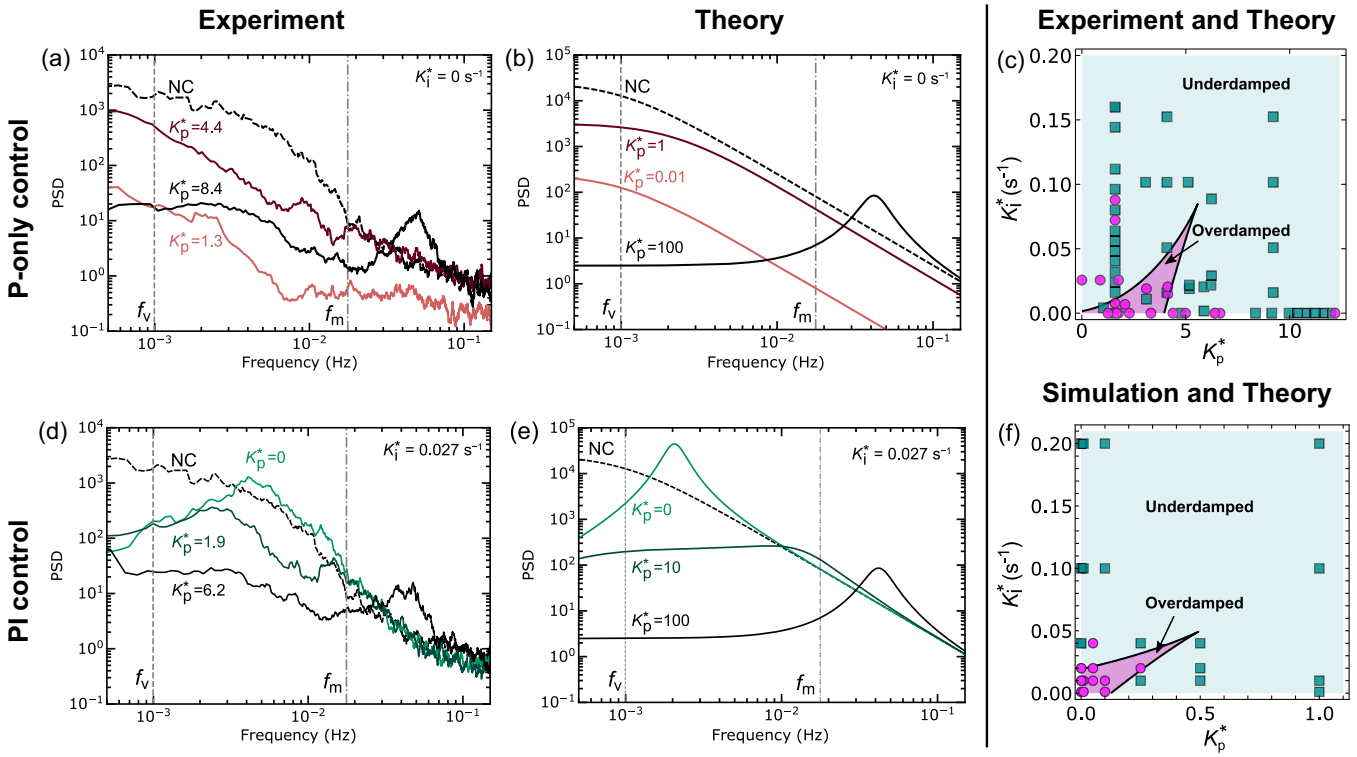

FIG. 5. Control gains influence the power spectra of mean speed v temporal fluctuations. (a),(b) Power spectra for zero integral gain ($K_i^* = 0$) and varying proportional gain (K_p^*) are presented for experimental observations and theoretical predictions, NC denotes "no control." (c) Theoretically predicted phase diagram compared with experimental data as a function of scaled gains K_p^* and K_i^*. (d),(e) Power spectra for nonzero integral gain ($K_i^* \neq 0$) with varying K_p^*. (f) Phase diagram comparing theory with nematohydrodynamic simulation results. Vertical lines for f_m and f_v in (a), (b), (d), and (e) represent $f_m = (2\pi\tau_m)^{-1}$ and $f_v = (2\pi\tau_v)^{-1}$. When comparing to experiment in (b), (c), and (e), theory curves use $\tau_m = 9$ s and $\tau_v = 160$ s; when comparing to simulations in (f), we use $\tau_m = 5$ (dimensionless) and $\tau_v = 2.5$ (dimensionless). Data point symbols indicate oscillatory (cyan squares) or purely exponentially decaying autocorrelation functions (magenta circles); see details in Fig. S2 [74].

suitable for PI control. However, the practical criterion is the magnitude of deviations from the set point. In this context, the oscillatory deviations may remain small enough to satisfy control objectives. While we focused on steady-state behavior through the lens of power spectra, examining the full response of the system through the related transfer function could yield further insights [60].

We also compare nematohydrodynamic simulations to our analytical theory, finding excellent agreement [Fig. 5(f)]. As in experiment and theory, uncontrolled nematics in simulations exhibit Lorentzian behavior characterized by a single hydrodynamic timescale, τ_v (Fig. S3 [74]). τ_v found in simulations differs from experimental values, leading to a change in the phase boundaries [Fig. 5(c)]. Our estimates of τ_v and prescribed τ_m from the simulation produce a theoretical phase diagram that agrees with numerics, supporting our framing of the controlled system as a coupled set of linear ODEs that effectively bridge experimental and computational observations.

In active fluids, intrinsic activity influences both the mean speed and the magnitude of fluctuations. Thus, fluctuations scale with the steady-state applied light. This interplay between activity and control generates nonmonotonic changes in fluctuations under proportional-only control, a signature of regulating active materials through their intrinsic activity. The steady-state speed depends on K_p when $K_i = 0$ due to droop; see Fig. 3. At the lowest gains, the speed and fluctuations remain small due to weak activity [Fig. 5(a), $K_p^* = 1.3$]. As the gain increases to $K_p^* = 4.4$, both speed and fluctuations grow, reflecting the typical scaling with activity. However, strikingly, further increases in K_p^* cause fluctuations to decline. This nonmonotonic response arises because K_p^* plays two competing roles in relation to fluctuations. On one hand, increasing K_p^* increases the mean speed, naturally amplifying activity-driven fluctuations. On the other hand, larger K_p^* strongly penalizes deviations from the set point. For small gains, the former mechanism dominates, while for large gains, the damping of fluctuations due to control overrides the activity-driven fluctuations.

Our theoretical model replicates the same nonmonotonic trend by letting the amplitude of the system's intrinsic fluctuations scale with the K_p^*-dependent steady state, such

that $\eta \sim \sqrt{K_p^*/(1+K_p^*)}$. Increasing the gain from $K_p^* = 0.01$ to 1 increases the amplitude across all frequencies [Fig. 5(b)]. Further increasing the gain to $K_p^* = 100$ decreases the amplitude and leads to the emergence of a peak, as discussed earlier. Integral control suppresses this trend, thus confirming that droop is necessary for nonmonotonic behavior [Figs. 5(d) and 5(e)]. These observations illustrate how control interacts with the intrinsic fluctuations of an active nematic, shaping their amplitude in a way that naturally emerges from the material's activity.

III. DISCUSSION AND CONCLUSIONS

A prominent feature of active nematic turbulence is the tight coupling between spatial and temporal characteristics [75]. We focused only on the temporal response by analyzing the coarse-grained flow speeds. This approach revealed significant impacts on the temporal structure of the flow (Fig. 5). Given the expected coupling, future work should consider if this impact is imprinted on the spatial structure, which could open new avenues for employing control strategies. The proposed coarse-grained linear model represents a significant simplification of the full nematohydrodynamic-controller system. We assumed that motor-binding kinetics dominanted the time lag. However, time lags are also introduced through the delays in the control hardware and software itself, which includes finite time required for velocity measurements, and the delays between frame acquisitions and processing time; all told, the cycle takes ~3 s [Fig. 1(a)]. Consequently, the magnitude of applied light reflects a past configuration of the system. Our current experimental setup makes it challenging to further decrease the time of the control loop; however, a systematic exploration of increased time lags would be informative. This may explain discrepancies between theory and experiment. For example, when compared to experiment, theory required much larger K_p values to produce a prominent peak in the power spectra [Figs. 5(a) and 5(b)].

The susceptibility of active nematics to light was quantified by the proportionality constant β, which varied from sample to sample and drifted over time by a factor of 2. Reliable feedback control without precise knowledge of β is possible, but its uncertainty leads to errors in our ability to report systematic changes in dynamics. For example, the data points in the phase diagram [Fig. 5(c)] shift by coordinate rescaling, since both K_i^* and K_p^* depend linearly on β. The variation of other model parameters, such as the time constants, is less characterized. To convey the sensitivity of the model predictions to such parameters, we show how the transition to underdamped behavior shifts with $\tau_{v,m}$ (Fig. S4 [74]).

With motile topological defects and chaotic fluid flows, 2D active nematics evoke many control possibilities. We established an experimental platform for autonomously regulating a simple, coarse-grained property of the system, its mean speed. However, in this realization, we have underutilized the actuatable and observable degrees of freedom available. This establishes a challenge to employ control theory or reinforcement learning to elicit more complex goals [47,48,51,52,56–58,76–79]. There remain theoretical and technical challenges in implementing model-based spatiotemporal control of active systems in real time. First, while nematohydrodynamic models recreate important statistical properties of active fluids, they can fail at granular predictions of material flows in microtubule-based nematics [25,47,49,51,80]. Thus, feedforward control maneuvers proposed in previous works face complications. Recalculating control policies iteratively in a model-predictive control framework using updated state information is a standard approach for overcoming poor models. However, this tactic significantly increases the computational burden of already taxing partial differential equation-constrained optimization. A fully realized model-based spatiotemporal controller for active nematics will likely utilize a combination of theoretical [80] and data-driven model improvements [81,82], some form of model reduction to reduce state and controller degrees of freedom [52], and leverage high-performance computing in concert. We note that systems that exhibit light-induced cross-linking and contractility may be more straightforward to control using inverse design with available models [44,45], as they lack the chaotic dynamics exhibited by extensile active nematics.

Like active reconstituted materials, biological systems engineered with optogenetic constructs are poised to use model-based strategies for spatiotemporal control. For example, exogenously patterning actomyosin contraction in embryonic monolayers has proven effective for steering in-plane cellular flows and driving out-of-plane buckling [83–90]. Building on these successes, inverse problem frameworks, especially those informed by advances in modeling multicellular systems [5,91,92], present a powerful way to turn *ad hoc* methods into systematic strategies for achieving complex tissue-scale patterning objectives.

Often, controller complexity is dictated by the control goal. Spatially averaged targets, such as control of defect density or mean speed of channel flows, are amenable to PI control, which, being model independent, is likely to succeed. However, more complex maneuvers are better tackled by leveraging models, such as the empirically motivated linear system through either model-predictive or linear-quadratic-regulatory frameworks [Eqs. (B1) and (B2)]. Model-predictive control is also a natural choice when nonlinearities are unavoidable. For example, while our kinesin-based system exhibits a simple relationship with light, other active systems, such as actomyosin, exhibit nonmonotonic responses [93], which are more readily incorporated into model-predictive control. This jump in complexity requires estimates for unmeasured dynamics

(in our case, bound motor concentration, which is not directly observable) and other uncertainties (i.e., $\beta, \tau_v, \tau_m, \ldots$). For that reason, coarse-grained models are an ideal test bed for exploring the implementation of control theory, such as variational data assimilation and Kalman filters, which would be more challenging to prototype for spatiotemporal control goals.

In addition to these engineering challenges, steering active matter systems raises questions about the thermodynamic limits of control. An ongoing research topic is the mapping of equilibrium statistical mechanical concepts, such as the fluctuation dissipation theorem, to systems that break time-reversal symmetry and, further, understanding how control strategies differ between active and passive systems [55]. Two nontrivial features of our experiment warrant further investigation. First, the noise in our coarse-grained model is fundamentally tied to the active rather than the passive part of the system. For example, the amplitude of fluctuations scales with steady-state speed controlled by K_p [Fig. 4(a)]. Second, while at the macroscale light impacts activity, unilluminated motor proteins continue to hydrolyze ATP and process along microtubules. Furthermore, another contributor to the system's dissipation, the glucose-fueled recycling of adenosine diphosphate back to useful ATP [94], is also not affected by the light. Instead, by dimerizing motors, the light field adds microscopic constraints to the system, radically altering the nature of dissipation in the system to include macroscale fluid flows. Building minimal models that capture these details may expose underlying laws governing nonequilibrium biological materials and facilitate the construction of control strategies.

The PI feedback can stabilize active flows despite intrinsic athermal fluctuations, environmental perturbations, and biomolecular degradation. The long-term goal is to replace exogenous light control with endogenous biochemical networks [95–98]. Analyzing a system's response to optogenetic actuation provides insight into the rational design of intrinsic biochemical networks [99–102], especially in light of the inherent fluctuations in those signaling systems. Advances in synthetic biology suggest that embedding such feedback in active materials is feasible, paving the way for autonomous, self-regulating systems.

ACKNOWLEDGMENTS

We thank Dr. Shibani Dalal, Director of the Brandeis Biomaterial Facility, for help with protein purification, and Dr. Fernando Caballero for assistance with cluster computing. This work, including experiments and computation, was primarily supported by the U.S. Department of Energy, Office of Science, Office of Basic Energy Sciences under Award No. DE-SC0022291 (K. N., J. B., S. G., A. A., M. F. H., Z. D., S. F.); development of the analytical theory was supported by DOE BES No. DE-SC0022280 (M. M. N.). Computational resources were provided by the NSF ACCESS allocation TG-MCB090163 and the Brandeis HPCC, which is partially supported by the NSF through DMR-MRSEC 2011846 and OAC-1920147.

K. N., J. B., M. M. N., M. F. H., Z. D., and S. F. designed the research; K. N., S. G., Z. Z., M. M. N., and J. B. performed the research. K. N., J. B., A. A., S. G., and M. M. N. analyzed data; K. N., J. B., M. M. N., M. F. H., Z. D., and S. F. wrote the paper.

The authors declare no competing interests.

DATA AVAILABILITY

The data that support the findings of this article are openly available [103].

APPENDIX A: EXPERIMENTAL METHODS

We developed a system that integrates a 2D active nematic (AN) with both hardware and software to implement feedback control. The microtubule-based active nematic is actuated by light-sensitive kinesin-motor clusters. Control of the system is realized through varying the applied light emitted from a projector focused directly onto the sample stage [Fig. 1(a)]. The control loop's software uses the Pycromanager library to coordinate the various hardware components of the control system. Our routine collects fluorescence images of the AN, calculates the mean speed using a machine learning-based optical flow algorithm [Fig. 1(b)] [73], and updates the uniformly applied light intensity I of the projector according to Eq. (1) [Fig. 1(c)].

Samples are enclosed in rectangular chambers composed of glass whose bottom wall is coated with Rain-X to create a hydrophobic surface and whose top surface is grafted with polyacrylamide to create a hydrophilic surface. These chambers are about 1 mm tall and about 10×5 mm^2 in the sample plane. Fluorinated oil is flowed into the chamber. Following this, aqueous solutions containing microtubules, kinesin, polyethylene glycol depletant, ATP, oxygen scavengers, and ATP-regeneration components are flushed through, creating an oil layer beneath the aqueous sample. The details of the active sample are provided in SM Methods section [74] (see also Refs. [9,40,42,73,104,105] therein). Our implementation differs from previous realizations because the volume of the chamber is increased ∼10-fold to increase the capacity of phosphoenolpyruvate (PEP), which is the ATP precursor in our ATP-regenerative enzymatic system [43]. The sample is then centrifuged for 3 min to quickly concentrate the microtubule bundles at the oil-water interface and placed on the fluorescence microscope within the control system. High intensity light is applied to activate the bundles and pack them into a two-dimensional film. The active nematic

is imaged with fluorescence microscopy and the control system is then activated. Before feedback control is recorded, experimental calibration is performed to allow for interpretation of data and comparison to our theoretical predictions. We measure the minimum flow speed of the active nematic in the absence of applied light v_0, as well as the linear response as light is increased β.

APPENDIX B: THEORY

We frame our observations of both the steady-state mean behavior and its fluctuations by developing a minimal linear ordinary differential equation model describing the coarse-grained dynamics of the spatially averaged speed v and concentration of dimerized motors m such that

$$\dot{v} = -v/\tau_v + \gamma_v m + \eta(t), \tag{B1}$$

$$\dot{m} = (m_0 - m)/\tau_m + \gamma_m I. \tag{B2}$$

A key feature of this model is that the control input $I(t)$ does not act directly on v, but through the intermediate dynamics of motor activation. This model assumes an infinite pool of motors available for dimerization. While more complex models of light-activated materials built from cytoskeletal components have been recently explored [106], here we focus on the simplest case to minimize the number of parameters in the model and facilitate analytical calculations. In brief, Eq. (B1) considers that the average speed v can change in three ways. The term $-v/\tau_v$ represents the intrinsic relaxation dynamics of the active nematic that we measure empirically, $\gamma_v m$ represents activity driven acceleration, and $\eta(t)$ represents activity-driven noise. Equation (B2) considers that the motor concentration that drives the active nematic can vary for two reasons. The first, represented by $(m_0 - m)/\tau_m$, describes the dynamics of bound motors in the absence of light, with m_0 the amount of permanently bound motors, while $\gamma_m I$ describes how the motor concentration varies in the presence of light.

The response of the system is governed by timescales for hydrodynamic and motor dynamics $\tau_{v,m}$. The latter was measured previously $\tau_m \sim \mathcal{O}(10)$ s [43], and the former we gather from our experiments here by examining the power spectra and autocorrelation function of the uncontrolled system, $\tau_v \sim \mathcal{O}(100\text{–}1000)$ s. To compare theory to nematohydrodynamics, we also empirically measure the time constant $\tau_v = 2.5$ (dimensionless), with $\tau_m = 5$ (dimensionless) being prescribed. The model is driven by white noise $\eta(t)$. We note that when modeling the control of a system, noise often represents exogenous forcing. In our case, the dominant contributor of noise is athermal and intrinsic to the active system itself, and, as such, we will subsequently let the amplitude of the noise scale with activity.

Finally, we introduce the proportionality coefficients $\gamma_{m,v}$. Their exact values are unimportant for the steady-state behavior of the system (average behavior and fluctuations) because, as we will see shortly, they depend only on a group of parameters coinciding with the experimentally measurable constant β, introduced below.

We first consider features predicted by this model of the limiting case of proportional-only control, e.g., $K_\mathrm{i} = 0$. For proportional-only control, we solve Eqs. (B1) and (B2) for the steady-state speed with $I = K_\mathrm{p}(v_\mathrm{set} - v)$ and find

$$\frac{v_\mathrm{ss}}{v_\mathrm{set}} = \frac{(\beta K_\mathrm{p} + v_0/v_\mathrm{set})}{(1 + \beta K_\mathrm{p})}, \tag{B3}$$

where β is the measured proportionality between applied light and velocity at steady state $v_\mathrm{ss} \sim \beta I_\mathrm{ss}$ and is defined in terms of model coefficients $\beta \equiv \tau_v \tau_m \gamma_v \gamma_m$. $v_0 \equiv m_0 \tau_m \gamma_v$ is the measured dark speed. To facilitate comparison between experiment for which $v_0 \neq 0$ and simulation, $v_0 = 0$, we rearrange Eq. (B3) and define a dimensionless steady-state speed accounting for the offset,

$$v^*_\mathrm{ss} \equiv \frac{v_\mathrm{ss}}{v_\mathrm{set}} - \frac{v_0}{v_\mathrm{set}} \frac{1}{1 + K^*_\mathrm{p}} = \frac{K^*_\mathrm{p}}{1 + K^*_\mathrm{p}}, \tag{B4}$$

where $K^*_\mathrm{p} = \beta K_\mathrm{p}$ is the dimensionless gain.

To compare our measurements of the fluctuations of the average speed, we examine the frequency response of the model Eqs. (1), (B1), and (B2) subject to white noise η. As mentioned above, we posit that the dominant source of fluctuations arises from the active hydrodynamic flows, so we let the noise drive the system at the level of the velocity dynamics, Eq. (B1). To account for the impact of droop on these intrinsic fluctuations, we let the amplitude scale with the square root of the steady-state mean speed [Eq. (B4)], such that $\eta \sim \sqrt{v^*_\mathrm{ss}} \sim \sqrt{K^*_\mathrm{p}/(1 + K^*_\mathrm{p})}$. It is straightforward to show that for $K^*_\mathrm{i} \neq 0$, $v^*_\mathrm{ss} = 1$.

We next consider steady-state fluctuations. Taking the Fourier transform of all functions $F(\omega) = \int_{-\infty}^{\infty} \mathrm{d}t e^{-i\omega t} f(t)$ and solving the resulting linear system for the transformed velocity $V(\omega)$ gives

$$V(\omega) = H \frac{i\omega\tau_v(1 + i\omega\tau_m)}{K^*_\mathrm{i} + i\omega K^*_\mathrm{p} + i\omega(1 + i\omega\tau_m)(1 + i\omega\tau_v)}, \tag{B5}$$

where H is the amplitude of the white noise, and, as in previous calculations, the unknown factors $\gamma_{v,m}$ are absorbed into the experimentally measurable factor β, and $K^*_\mathrm{p}, K^*_\mathrm{i} = \beta K_\mathrm{p}, \beta K_\mathrm{i}$ are the scaled gains. Plotting $|V|^2$ yields predictions as a function of parameters $\{K^*_\mathrm{p}, K^*_\mathrm{i}, \tau_v, \tau_m\}$. Finally, we identify the criterion for oscillations by solving the characteristic equation for the eigenvalues of Eqs. (1), (B1), and (B2),

$$\lambda^3 + \lambda^2\left(\frac{1}{\tau_m} + \frac{1}{\tau_v}\right) + \lambda\frac{1 + K_\mathrm{p}^*}{\tau_m\tau_v} + K_\mathrm{i}^*\frac{1}{\tau_m\tau_v} = 0, \quad \text{(B6)}$$

and finding conditions where $\mathrm{Im}(\lambda) > 0$.

APPENDIX C: NUMERICAL METHODS

We compare experimental observations to a standard model of nematohydrodynamics subject to PI control and aforementioned motor-binding dynamics. For simplicity, we set the active stress strength equal to the active motor concentration m. Nematic order is represented by the traceless and symmetric second order tensor $\mathbf{Q} = s[\mathbf{n}\otimes\mathbf{n} - \mathbf{I}/2]$, where $\mathbf{n}$ is the nematic orientation and $s = \sqrt{2\mathbf{Q}:\mathbf{Q}}$ is the degree of order. Momentum conservation, in the limit of low inertia and vanishing passive liquid crystalline stresses, and incompressibility govern the fluid flow $\mathbf{v}$ and hydrostatic pressure p such that

$$\begin{aligned}\partial_t\mathbf{Q} + \mathbf{v}\cdot\nabla\mathbf{Q} + [\mathbf{\Omega}, \mathbf{Q}] - \lambda\mathbf{E} &= (1 - s^2)\mathbf{Q} + K\nabla^2\mathbf{Q},\\ \nabla^2\mathbf{v} - \nabla p - m\nabla\cdot\mathbf{Q} - \xi\mathbf{v} &= 0,\\ \nabla\cdot\mathbf{v} &= 0,\end{aligned} \quad \text{(C1)}$$

where $2\Omega_{ij} = \partial_j v_i - \partial_i v_j$ and $2E_{ij} = \partial_j v_i + \partial_i v_j$ are, respectively, the antisymmetric and symmetric parts of the flow field gradient, $[\cdots]$ is the commutator. In our study, we fix the strength of substrate friction $\xi = 0.01$, nematic elasticity $K = 4$, and flow alignment $\lambda = 1$.

Equations (C1) are coupled to the same ordinary differential equations governing the control input I and active motors m in our coarse-grained model, Eqs. (1) and (B2). Since we uniformly apply control to the entire domain, we can ignore convection and diffusion processes in m. We fix $\tau_m = 5$ and $\gamma_m = 0.2$ in our simulations. We solve the coupled system of PDEs, ordinary differential equation, and control law using the spectral solver CUPSS [107] in a domain size of 128×128 with 128×128 spatial modes.

[1] J. Sedzinski, M. Biro, A. Oswald, J.-Y. Tinevez, G. Salbreux, and E. Paluch, *Polar actomyosin contractility destabilizes the position of the cytokinetic furrow*, Nature (London) **476**, 462 (2011).

[2] S. R. Naganathan, S. Fürthauer, M. Nishikawa, F. Jülicher, and S. W. Grill, *Active torque generation by the actomyosin cell cortex drives left–right symmetry breaking*, eLife **3**, e04165 (2014).

[3] J. Brugués and D. Needleman, *Physical basis of spindle self-organization*, Proc. Natl. Acad. Sci. U.S.A. **111**, 18496 (2014).

[4] A. Steffen, T. E. Stradal, and K. Rottner, *Signalling pathways controlling cellular actin organization*, Actin Cytoskeleton 153 (2017).

[5] S. J. Streichan, M. F. Lefebvre, N. Noll, E. F. Wieschaus, and B. I. Shraiman, *Global morphogenetic flow is accurately predicted by the spatial distribution of myosin motors*, eLife **7**, e27454 (2018).

[6] F. Nedelec, T. Surrey, A. C. Maggs, and S. Leibler, *Self-organization of microtubules and motors*, Nature (London) **389**, 305 (1997).

[7] J. Tabony, N. Glade, J. Demongeot, and C. Papaseit, *Biological self-organization by way of microtubule reaction-diffusion processes*, Langmuir **18**, 7196 (2002).

[8] V. Schaller, C. Weber, C. Semmrich, E. Frey, and A. R. Bausch, *Polar patterns of driven filaments*, Nature (London) **467**, 73 (2010).

[9] T. Sanchez, D. T. Chen, S. J. DeCamp, M. Heymann, and Z. Dogic, *Spontaneous motion in hierarchically assembled active matter*, Nature (London) **491**, 431 (2012).

[10] M. P. Murrell and M. L. Gardel, *F-actin buckling coordinates contractility and severing in a biomimetic actomyosin cortex*, Proc. Natl. Acad. Sci. U.S.A. **109**, 20820 (2012).

[11] J. Alvarado, M. Sheinman, A. Sharma, F. C. MacKintosh, and G. H. Koenderink, *Molecular motors robustly drive active gels to a critically connected state*, Nat. Phys. **9**, 591 (2013).

[12] P. J. Foster, S. Fürthauer, M. J. Shelley, and D. J. Needleman, *Active contraction of microtubule networks*, eLife **4**, e10837 (2015).

[13] J. Berezney, B. L. Goode, S. Fraden, and Z. Dogic, *Extensile to contractile transition in active microtubule–actin composites generates layered asters with programmable lifetimes*, Proc. Natl. Acad. Sci. U.S.A. **119**, e2115895119 (2022).

[14] B. Lemma, N. P. Mitchell, R. Subramanian, D. J. Needleman, and Z. Dogic, *Active microphase separation in mixtures of microtubules and tip-accumulating molecular motors*, Phys. Rev. X **12**, 031006 (2022).

[15] G. Livne, S. Gat, S. Armon, and A. Bernheim-Groswasser, *Self-assembled active actomyosin gels spontaneously curve and wrinkle similar to biological cells and tissues*, Proc. Natl. Acad. Sci. U.S.A. **121**, e2309125121 (2024).

[16] H. Levine and D. I. Goldman, *Physics of smart active matter: Integrating active matter and control to gain insights into living systems*, Soft Matter **19**, 4204 (2023).

[17] A. J. Tan, E. Roberts, S. A. Smith, U. A. Olvera, J. Arteaga, S. Fortini, K. A. Mitchell, and L. S. Hirst, *Topological chaos in active nematics*, Nat. Phys. **15**, 1033 (2019).

[18] C. G. Wagner, M. M. Norton, J. S. Park, and P. Grover, *Exact coherent structures and phase space geometry of preturbulent 2D active nematic channel flow*, Phys. Rev. Lett. **128**, 028003 (2022).

[19] C. G. Wagner, R. H. Pallock, J. S. Park, M. M. Norton, and P. Grover, *Exploring regular and turbulent flow states in active nematic channel flow via exact coherent structures and their invariant manifolds*, Phys. Rev. Fluids **8**, 124401 (2023).

[20] J. Alvarado, E. Teich, D. A. Sivak, and J. Bechhoefer, *Optimal control in soft and active matter*, arXiv:2504.08676.

[21] H. Wioland, F. G. Woodhouse, J. Dunkel, J. O. Kessler, and R. E. Goldstein, *Confinement stabilizes a bacterial suspension into a spiral vortex*, Phys. Rev. Lett. **110**, 268102 (2013).

[22] E. Lushi, H. Wioland, and R. E. Goldstein, *Fluid flows created by swimming bacteria drive self-organization in confined suspensions*, Proc. Natl. Acad. Sci. U.S.A. **111**, 9733 (2014).
[23] F. C. Keber, E. Loiseau, T. Sanchez, S. J. DeCamp, L. Giomi, M. J. Bowick, M. C. Marchetti, Z. Dogic, and A. R. Bausch, *Topology and dynamics of active nematic vesicles*, Science **345**, 1135 (2014).
[24] K.-T. Wu, J. B. Hishamunda, D. T. Chen, S. J. DeCamp, Y.-W. Chang, A. Fernández-Nieves, S. Fraden, and Z. Dogic, *Transition from turbulent to coherent flows in confined three-dimensional active fluids*, Science **355**, eaal1979 (2017).
[25] A. Opathalage, M. M. Norton, M. P. N. Juniper, B. Langeslay, S. A. Aghvami, S. Fraden, and Z. Dogic, *Self-organized dynamics and the transition to turbulence of confined active nematics*, Proc. Natl. Acad. Sci. U.S.A. **116**, 4788 (2019).
[26] J. Hardoüin, R. Hughes, A. Doostmohammadi, J. Laurent, T. Lopez-Leon, J. M. Yeomans, J. Ignés-Mullol, and F. Sagués, *Reconfigurable flows and defect landscape of confined active nematics*, Commun. Phys. **2**, 121 (2019).
[27] S. Uplap, M. F. Hagan, and A. Baskaran, *Design principles for transporting vesicles with enclosed active particles*, Europhys. Lett. **143**, 67001 (2023).
[28] Y. Fily, A. Baskaran, and M. F. Hagan, *Dynamics of self-propelled particles under strong confinement*, Soft Matter **10**, 5609 (2014).
[29] Z. Fazli and A. Naji, *Active particles with polar alignment in ring-shaped confinement*, Phys. Rev. E **103**, 022601 (2021).
[30] P. Iyer, G. Gompper, and D. A. Fedosov, *Dynamic shapes of floppy vesicles enclosing active Brownian particles with membrane adhesion*, Soft Matter **19**, 3436 (2023).
[31] F. L. Memarian, D. Hammar, Md Mainul Hasan Sabbir, M. Elias, K. A. Mitchell, and L. S. Hirst, *Controlling chaos: periodic defect braiding in active nematics confined to a cardioid*, Phys. Rev. Lett. **132**, 228301 (2024).
[32] I. Vélez-Cerón, P. Guillamat, F. Sagués, and J. Ignés-Mullol, *Probing active nematics with in situ microfabricated elastic inclusions*, Proc. Natl. Acad. Sci. U.S.A. **121**, e2312494121 (2024).
[33] I. Vélez-Ceron, R. C. V. Coelho, P. Guillamat, M. T. da Gama, F. Sagués, and J. Ignés-Mullol, *Active nematic pumps*, arXiv:2407.09960.
[34] P. Guillamat, J. Ignés-mullol, and F. Sagués, *Control of active liquid crystals with a magnetic field*, Proc. Natl. Acad. Sci. U.S.A. **113**, 5498 (2016).
[35] K. Thijssen, D. A. Khaladj, S. A. Aghvami, M. A. Gharbi, S. Fraden, J. M. Yeomans, L. S. Hirst, and T. N. Shendruk, *Submersed micropatterned structures control active nematic flow, topology, and concentration*, Proc. Natl. Acad. Sci. U.S.A. **118**, e2106038118 (2021).
[36] T. E. Bate, M. E. Varney, E. H. Taylor, J. H. Dickie, C.-C. Chueh, M. M. Norton, and K.-T. Wu, *Self-mixing in microtubule-kinesin active fluid from nonuniform to uniform distribution of activity*, Nat. Commun. **13**, 6573 (2022).
[37] M. Schuppler, F. C. Keber, M. Kröger, and A. R. Bausch, *Boundaries steer the contraction of active gels*, Nat. Commun. **7**, 13120 (2016).
[38] I. Linsmeier, S. Banerjee, P. W. Oakes, W. Jung, T. Kim, and M. P. Murrell, *Disordered actomyosin networks are sufficient to produce cooperative and telescopic contractility*, Nat. Commun. **7**, 12615 (2016).
[39] D. P. Rivas, T. N. Shendruk, R. R. Henry, D. H. Reich, and R. L. Leheny, *Driven topological transitions in active nematic films*, Soft Matter **16**, 9331 (2020).
[40] T. D. Ross, H. J. Lee, Z. Qu, R. A. Banks, R. Phillips, and M. Thomson, *Controlling organization and forces in active matter through optically defined boundaries*, Nature (London) **572**, 224 (2019).
[41] R. Zhang, S. A. Redford, P. V. Ruijgrok, N. Kumar, A. Mozaffari, S. Zemsky, A. R. Dinner, V. Vitelli, Z. Bryant, M. L. Gardel, and J. J. de Pablo, *Spatiotemporal control of liquid crystal structure and dynamics through activity patterning*, Nat. Mater. **20**, 875 (2021).
[42] L. M. Lemma, M. Varghese, T. D. Ross, M. Thomson, A. Baskaran, and Z. Dogic, *Spatio-temporal patterning of extensile active stresses in microtubule-based active fluids*, PNAS Nexus **2**, pgad130 (2023).
[43] Z. Zarei, J. Berezney, A. Hensley, L. Lemma, N. Senbil, Z. Dogic, and S. Fraden, *Light-activated microtubule-based two-dimensional active nematic*, Soft Matter **19**, 6691 (2023).
[44] F. Yang, S. Liu, H. J. Lee, R. Phillips, and M. Thomson, *Dynamic flow control through active matter programming language*, Nat. Mater. **24**, 615 (2025).
[45] X. Lei, C. Floyd, L. C. Ferrer, T. Chakrabortty, N. Chandrasekharan, A. R. Dinner, S. Coyle, J. Honts, and S. Bhamla, *Light-induced assembly and repeatable actuation in Ca^{2+}-driven chemomechanical protein networks*, 10.1101/2025.03.03.641304.
[46] T. Litschel, D. Vavylonis, and D. A. Weitz, *3D printing cytoskeletal networks: ROS-induced filament severing leads to surge in actin polymerization*, 10.1101/2025.03.19.644260.
[47] M. M. Norton, P. Grover, M. F. Hagan, and S. Fraden, *Optimal control of active nematics*, Phys. Rev. Lett. **125**, 178005 (2020).
[48] S. Shankar, V. Raju, and L. Mahadevan, *Optimal transport and control of active drops*, Proc. Natl. Acad. Sci. U.S.A. **119**, e2121985119 (2022).
[49] C. Sinigaglia, F. Braghin, and M. Serra, *Optimal control of short-time attractors in active nematics*, Phys. Rev. Lett. **132**, 218302 (2024).
[50] S. Ghosh, C. Joshi, A. Baskaran, and M. F. Hagan, *Spatiotemporal control of structure and dynamics in a polar active fluid*, arXiv:2405.07942.
[51] S. Ghosh, A. Baskaran, and M. F. Hagan, *Achieving designed texture and flows in bulk active nematics using optimal control theory*, arXiv:2408.14596.
[52] S. Shankar, L. V. D. Scharrer, M. J. Bowick, and M. C. Marchetti, *Design rules for controlling active topological defects*, Proc. Natl. Acad. Sci. U.S.A. **121**, e2400933121 (2024).
[53] E. Schneider and H. Stark, *Optimal steering of a smart active particle*, Europhys. Lett. **127**, 64003 (2019).

[54] B. Liebchen and H. Löwen, *Optimal navigation strategies for active particles*, Europhys. Lett. **127**, 34003 (2019).
[55] L. K. Davis, K. Proesmans, and É. Fodor, *Active matter under control: Insights from response theory*, Phys. Rev. X **14**, 011012 (2024).
[56] M. J. Falk, V. Alizadehyazdi, H. Jaeger, and A. Murugan, *Learning to control active matter*, Phys. Rev. Res. **3**, 033291 (2021).
[57] C. Floyd, A. R. Dinner, and S. Vaikuntanathan, *Tailoring interactions between active nematic defects with reinforcement learning*, Soft Matter **21**, 4488 (2025).
[58] S. Chennakesavalu, S. K. Manikandan, F. Hu, and G. M. Rotskoff, *Adaptive nonequilibrium design of actin-based metamaterials: Fundamental and practical limits of control*, Proc. Natl. Acad. Sci. U.S.A. **121**, e2310238121 (2024).
[59] T. Quah, S. C. Takatori, and J. B. Rawlings, *Learning continuum-level closures for control of interacting active particles*, arXiv:2501.18809.
[60] J. Bechhoefer, *Control Theory for Physicists* (Cambridge University Press, Cambridge, England, 2021).
[61] J. Palacci, S. Sacanna, A. P. Steinberg, D. J. Pine, and P. M. Chaikin, *Living crystals of light-activated colloidal surfers*, Science **339**, 936 (2013).
[62] A. Aubret, M. Youssef, S. Sacanna, and J. Palacci, *Targeted assembly and synchronization of self-spinning microgears*, Nat. Phys. **14**, 1114 (2018).
[63] G. Frangipane, D. Dell'Arciprete, S. Petracchini, C. Maggi, F. Saglimbeni, S. Bianchi, G. Vizsnyiczai, M. L. Bernardini, and R. Di Leonardo, *Dynamic density shaping of photokinetic E. coli*, eLife **7**, e36608 (2018).
[64] J. Arlt, V. A. Martinez, A. Dawson, T. Pilizota, and W. C. Poon, *Painting with light-powered bacteria*, Nat. Commun. **9**, 768 (2018).
[65] A. Repula, C. Gates, J. C. Cameron, and I. I. Smalyukh, *Photosynthetically-powered phototactic active nematic liquid crystal fluids and gels*, Commun. Mater. **5**, 37 (2024).
[66] G. Volpe, I. Buttinoni, D. Vogt, H.-J. Kümmerer, and C. Bechinger, *Microswimmers in patterned environments*, Soft Matter **7**, 8810 (2011).
[67] Z. Huang, T. Omori, and T. Ishikawa, *Active droplet driven by a collective motion of enclosed microswimmers*, Phys. Rev. E **102**, 022603 (2020).
[68] K. Villa and M. Pumera, *Fuel-free light-driven micro/nanomachines: Artificial active matter mimicking nature*, Chem. Soc. Rev. **48**, 4966 (2019).
[69] Z. Qu, D. Schildknecht, S. Shadkhoo, E. Amaya, J. Jiang, H. J. Lee, D. Larios, F. Yang, R. Phillips, and M. Thomson, *Persistent fluid flows defined by active matter boundaries*, Commun. Phys. **4**, 198 (2021).
[70] R. A. Simha and S. Ramaswamy, *Hydrodynamic fluctuations and instabilities in ordered suspensions of self-propelled particles*, Phys. Rev. Lett. **89**, 058101 (2002).
[71] S. P. Thampi, R. Golestanian, and J. M. Yeomans, *Instabilities and topological defects in active nematics*, Europhys. Lett. **105**, 18001 (2014).
[72] L. Giomi, M. J. Bowick, P. Mishra, R. Sknepnek, and M. Cristina Marchetti, *Defect dynamics in active nematics*, Phil. Trans. R. Soc. A **372**, 20130365 (2014).
[73] P. N. Tran, S. Ray, L. Lemma, Y. Li, R. Sweeney, A. Baskaran, Z. Dogic, P. Hong, and M. F. Hagan, *Deep-learning optical flow for measuring velocity fields from experimental data*, Soft Matter **20**, 7246 (2024).
[74] See Supplemental Material at http://link.aps.org/supplemental/10.1103/4hrx-6rdq for experimental methods, PI control implementation, autocorrelation analysis, supporting figures, and fluorescence microscopy movies of active nematic flows under various control conditions.
[75] R. Alert, A. Martínez-Calvo, and S. S. Datta, *Cellular sensing governs the stability of chemotactic fronts*, Phys. Rev. Lett. **128**, 148101 (2022).
[76] A. Lamtyugina, Y. Qiu, E. Fodor, A. R. Dinner, and S. Vaikuntanathan, *Thermodynamic control of activity patterns in cytoskeletal networks*, Phys. Rev. Lett. **129**, 128002 (2022).
[77] C. Floyd, A. R. Dinner, and S. Vaikuntanathan, *Learning to control non-equilibrium dynamics using local imperfect gradients*, arXiv:2404.03798.
[78] V. Krishnan, S. Sinha, and L. Mahadevan, *Hamiltonian bridge: A physics-driven generative framework for targeted pattern control*, arXiv:2410.12665.
[79] S. Sinha, V. Krishnan, and L. Mahadevan, *Optimal control of interacting active particles on complex landscapes*, arXiv:2311.17039.
[80] K. A. Mitchell, M. M. H. Sabbir, S. Ricarte, B. Klein, and D. A. Beller, *Modeling active nematics via the nematic locking principle*, arXiv:2506.20996.
[81] C. Joshi, S. Ray, L. M. Lemma, M. Varghese, G. Sharp, Z. Dogic, A. Baskaran, and M. F. Hagan, *Data-driven discovery of active nematic hydrodynamics*, Phys. Rev. Lett. **129**, 258001 (2022).
[82] M. Golden, R. O. Grigoriev, J. Nambisan, and A. Fernandez-Nieves, *Physically informed data-driven modeling of active nematics*, Sci. Adv. **9**, eabq6120 (2023).
[83] H. E. Johnson, N. J. Djabrayan, S. Y. Shvartsman, and J. E. Toettcher, *Optogenetic rescue of a patterning mutant*, Curr. Biol. **30**, 3414 (2020).
[84] R. M. Herrera-Perez, C. Cupo, C. Allan, A. Lin, and K. E. Kasza, *Using optogenetics to link myosin patterns to contractile cell behaviors during convergent extension*, Biophys. J. **120**, 4214 (2021).
[85] M. Herrera-Perez, C. Cupo, C. Allan, A. B. Dagle, and K. E. Kasza, *Optogenetic dissection of actomyosin-dependent mechanics underlying tissue fluidity*, https://www.biorxiv.org/content/10.1101/2021.11.07.467642v2.
[86] A. D. Countryman, C. A. Doherty, R. M. Herrera-Perez, and K. E. Kasza, *Endogenous OptoRhoGEFs reveal biophysical principles of epithelial tissue furrowing*, 10.1101/2024.05.12.593711.
[87] K. Suh, R. Thornton, P. E. Farahani, D. Cohen, and J. Toettcher, *Large-scale control over collective cell migration using light-controlled epidermal growth factor receptors*, 10.1101/2024.05.30.596676.
[88] S. Kumar, H. M. Beyer, M. Chen, M. D. Zurbriggen, and M. Khammash, *Image-guided optogenetic spatiotemporal tissue patterning using μ PatternScope*, Nat. Commun. **15**, 10469 (2024).
[89] N. A. Repina, H. J. Johnson, X. Bao, J. A. Zimmermann, D. A. Joy, S. Z. Bi, R. S. Kane, and D. V. Schaffer,

Optogenetic control of Wnt signaling models cell-intrinsic embryogenic patterning using 2D human pluripotent stem cell culture, Development **150**, 201386 (2023).

[90] H. M. Beyer, S. Kumar, M. Nieke, C. M. C. Diehl, K. Tang, S. Shumka, C. S. Koh, C. Fleck, J. A. Davies, M. Khammash, and M. D. Zurbriggen, *Genetically-stable engineered optogenetic gene switches modulate spatial cell morphogenesis in two- and three-dimensional tissue cultures*, Nat. Commun. **15**, 10470 (2024).

[91] M. Serra, G. Serrano Nájera, M. Chuai, A. M. Plum, S. Santhosh, V. Spandan, C. J. Weijer, and L. Mahadevan, *A mechanochemical model recapitulates distinct vertebrate gastrulation modes*, Sci. Adv. **9**, eadh8152 (2023).

[92] A. M. Plum, M. Serra, and C. J. Weijer, *Advances in mechanochemical modelling of vertebrate gastrulation*, Biochem. Soc. Trans. **53**, 871 (2025).

[93] S. A. Redford, J. Colen, J. L. Shivers, S. Zemsky, M. Molaei, C. Floyd, P. V. Ruijgrok, V. Vitelli, Z. Bryant, A. R. Dinner, and M. L. Gardel, *Motor crosslinking augments elasticity in active nematics*, Soft Matter **20**, 2480 (2024).

[94] P. J. Foster, J. Bae, B. Lemma, J. Zheng, W. Ireland, P. Chandrakar, R. Boros, Z. Dogic, D. J. Needleman, and J. J. Vlassak, *Dissipation and energy propagation across scales in an active cytoskeletal material*, Proc. Natl. Acad. Sci. U.S.A. **120**, e2207662120 (2023).

[95] H. Dehne, A. Reitenbach, and A. R. Bausch, *Reversible and spatiotemporal control of colloidal structure formation*, Nat. Commun. **12**, 6811 (2021).

[96] M. M. Norton and P. Grover, *Mechanochemical topological defects in an active nematic*, Phys. Rev. E **110**, 054605 (2024).

[97] R. Rajasekaran, C.-C. Chang, E. W. Weix, T. M. Galateo, and S. M. Coyle, *A programmable reaction-diffusion system for spatiotemporal cell signaling circuit design*, Cell **187**, 345 (2024).

[98] G. Leech, L. Melcher, M. Chiu, M. Nugent, S. Juliano, L. Burton, J. Kang, S. J. Kim, S. Roy, L. Farhadi, J. L. Ross, M. Das, M. J. Rust, and R. M. Robertson-Anderson, *Programming scheduled self-assembly of circadian materials*, Nat. Commun. **16**, 176 (2025).

[99] S. Kumar and M. Khammash, *Platforms for optogenetic stimulation and feedback control*, Front. Bioeng. Biotechnol. **10** (2022).

[100] T. Frei, C.-H. Chang, M. Filo, A. Arampatzis, and M. Khammash, *A genetic mammalian proportional–integral feedback control circuit for robust and precise gene regulation*, Proc. Natl. Acad. Sci. U.S.A. **119**, e2122132119 (2022).

[101] J.-B. Lugagne and M. J. Dunlop, *Cell-machine interfaces for characterizing gene regulatory network dynamics*, Curr. Opin. Syst. Biol. **14**, 1 (2019).

[102] C. Carrasco-López, S. A. García-Echauri, T. Kichuk, and J. L. Avalos, *Optogenetics and biosensors set the stage for metabolic cybergenetics*, Curr. Opin. Biotechnol. **65**, 296 (2020).

[103] K. Nishiyama, J. Berezney, M. Norton, A. Aggarwal, S. Ghosh, Z. Zarei, M. Hagan, Z. Dogic, and S. Fraden, *Dataset from closed-loop control of active nematic flows*, Zenodo, 10.5281/zenodo.14720865 (2025).

[104] M. Castoldi and A. V. Popov, *Purification of brain tubulin through two cycles of polymerization–depolymerization in a high-molarity buffer*, Protein Expression Purif. **32**, 83 (2003).

[105] G. Guntas, R. A. Hallett, S. P. Zimmerman, T. Williams, H. Yumerefendi, J. E. Bear, and B. Kuhlman, *Engineering an improved light-induced dimer (iLID) for controlling the localization and activity of signaling proteins*, Proc. Natl. Acad. Sci. U.S.A. **112**, 112 (2015).

[106] F. Yang, S. Liu, H. J. Lee, R. Phillips, and M. Thomson, *Geometry-dependent defect merging induces bifurcated dynamics in active networks*, Phys. Rev. Res. **7**, L042006 (2025).

[107] F. Caballero, *CUPSS: A package for pseudo-spectral integration of stochastic PDEs*, arXiv:2405.02410.